Drylines in Southern Africa: Rediscovering the Congo Air Boundary

Article

www.reading.ac.uk/centaur

CentAUR

Central Archive at the University of Reading

Reading's research outputs online

Drylines in Southern Africa: Rediscovering the Congo Air Boundary

EMMA HOWARD AND RICHARD WASHINGTON

School of Geography and the Environment, University of Oxford, Oxford, United Kingdom

ABSTRACT

Projected rainfall decline in southern Africa is likely to be highly sensitive to subtleties in the local atmospheric circulation. In an effort to understand the regional circulation complexities, a novel algorithm is developed to identify the Congo air boundary (CAB) in ERA-5, a high-resolution reanalysis dataset. The CAB, a forgotten feature of the circulation, is defined in the austral spring and early summer, using surface humidity gradients and near-surface wind convergence lines, and it is found to be an indicator of the location of the southern edge of the African rain belt. A related convergence-line and dryline feature, described in this paper as the Kalahari discontinuity (KD), is also identified. It is established that either a dryline CAB or KD is present in southern Africa for over 95% of days between August and December, with arc lengths typically exceeding 10°. The seasonal and diurnal cycles of the CAB and the KD are presented, and their prevalence in station observational data is confirmed. The interannual variability of the CAB latitude and detection frequency is found to explain at least 55% of interannual spring rainfall variability in southern Africa between 15° to 25°S. Links are established with the Angola and Kalahari heat lows and tropical temperate trough events.

1. Introduction

Southern Africa is one of the few inhabited regions of the world in which CMIP5 models project a robust decline in annual rainfall under future warming scenarios (IPCC 2013, p. 1061). In this region, the maximum magnitudes of projected rainfall decline occur in a latitudinal band between 10° and 20°S, primarily in the months of October, November, and December. The RCP8.5 multimodel mean places rainfall decline at 6 mm per month per degree of warming (Lazenby et al. 2018). As southern Africa is highly dependent on rainfall for water, energy, and food production (Conway et al. 2015), these rainfall changes have the potential for dire consequences. Further investigations into the mechanisms and uncertainty associated with these projections are required to prepare for life in a warmer world.

The rainfall decline over southern Africa has been attributed to a delayed rainy season onset, causing a shortening in the overall duration in the rain season (Dunning et al. 2018). The onset of the rains results from the seasonal shift in the African rain belt, which moves slowly south through the continent, with the onset of rainfall occurring earlier farther north and later farther south (Dunning et al. 2016). A wide, north–south-oriented gradient in onset date is present over most of Angola, Zambia, and southeast of the Democratic Republic of the Congo (DRC) (Dunning et al. 2016). However, the dynamics of the southern shift in the rain belt in spring and early summer are not fully understood (Nicholson 2018), and further investigation of the present day seasonal cycle is required before the mechanisms of future change may be fully characterized.

It is apparent from Fig. 1 that in the climatological seasonal cycle, the rain belt (green) is collocated with a broad band of near-saturated relative humidity (blue contours). The humidity band moves north and south with the seasonal cycle of the rain belt. On the northern and southern edges of the rain belt, the humidity decreases rapidly, particularly from August to November in on the southern edge, and from March to June on the

Climatological Hovmoller of Rainfall, Surface Temperature and Surface Specific Humidity
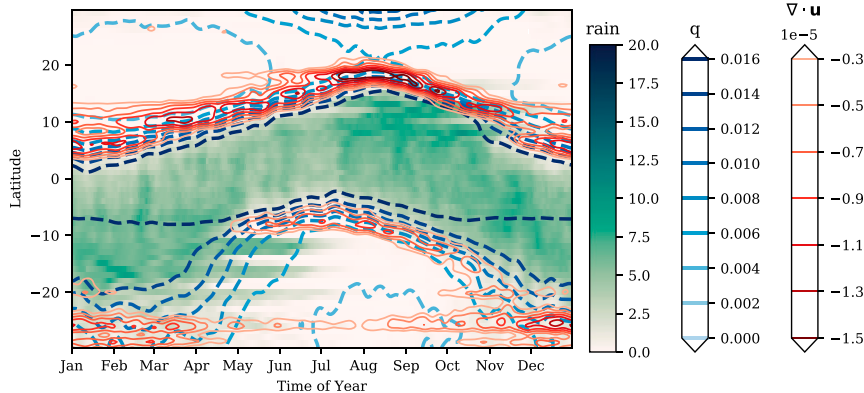

FIG. 1. Climatology progression of the southern African rain band, averaged between 18° and 23°E. Green colors: rainfall (mm day^{-1}; NOAA 2012). Dashed blue contours: specific humidity at 2 m AGL (kg kg^{-1}). Solid red contours: Wind convergence 10 m AGL (s^{-1}).

northern edge. These strong humidity gradients are often collocated with strong surface wind convergence (red contours). In this paper, we show that the Southern Hemisphere spring wind convergence and humidity gradients are the climatological aggregation of the Congo air boundary (CAB). We identify the seasonal migration of the CAB as a key process that heralds the southward shift of the African rain belt. We use reanalysis data to establish a baseline against which historical climate models may be compared in future studies.

Spring and summer rainfall in tropical southern Africa, and in particular in Angola and Zambia, has long been understood to be associated with the CAB (e.g., Torrance 1979). The CAB, also referred to as the Zaire air boundary, is traditionally defined as the location where the low-level westerlies (LLW), which originate as recurved Atlantic southeasterlies, meet with the easterly Indian Ocean trade winds at the surface (Taljaard 1972; Torrance 1979). Taljaard (1986) listed the placement of the interocean trough as one of the 10 factors that play a key role in the weather over southern Africa. Both Torrance (1979) and Leroux (2001) point out that the converging air masses differ strongly in humidity, the LLW being close to saturation after their journey over the Congo rain forest, and the easterly trades having been "continentalized" and dried out over the great escarpment.

However, although the CAB was frequently discussed in the 1970s and 1980s when weather forecasters doubled as climate researchers, it has receded in the academic literature of southern African present-day climatology in the last two decades while prevailing in East African and paleoclimate literature (e.g., Nicholson 1996; Kizza et al. 2009; Tierney et al. 2011;

Junginger et al. 2014). As far as the authors are aware, no attempts have been made to identify the CAB in reanalysis datasets or in global or regional atmospheric models. This may in part be due to an inability of reanalysis and models to fully resolve the CAB, owing to their low resolution. However, the recent publication of the ERA-5 reanalysis dataset, at 30-km resolution, provides a solution to this problem.

This paper intends to fill this gap by developing an algorithm to detect the CAB in daily ERA-5 reanalysis. Two formulations are presented, one that identifies convergence lines and the other that tracks drylines, and their relative robustness is discussed. A second surface convergence-line/dryline system, the Kalahari discontinuity (KD), is also identified and studied. The diurnal and seasonal cycles of various properties of the CAB and the KD are considered, and the CAB's vital importance for regional precipitation is verified. The reanalysis-based CAB is compared favorably to literature of the twentieth century. A link to the formation of tropical temperate troughs (TTT) is discussed.

The remainder of this paper will proceed as follows. The next section provides a comprehensive review of the twentieth-century literature relating to the CAB, and section 3 compares this literature with climatological means and sample days from ERA-5. In section 4, we develop an algorithm to identify the CAB and the KD using techniques adapted from image processing. In section 5, we analyze the seasonal cycle and properties of the CAB and the KD in reanalysis and automatic weather station (AWS) data. A moisture budget analysis is used to study diurnal cycle of the maintenance of the sharp humidity gradient in section 6. In section 7 we examine the interannual influence of the CAB on

rainfall, and its relationship with TTTs. The final section presents our conclusions.

2. Literature review

The concept of the CAB emerged in the scientific literature during attempts to describe the intertropical convergence zone (ITCZ) over the African continent. The ITCZ is traditionally defined as the region in which the trade winds from the Northern and Southern Hemispheres converge (e.g., van Heerden and Taljaard 1998). However, the complexity of African climate leads competing processes to create zonally asymmetric wind patterns that do not fit with the ITCZ paradigm (Nicholson 2018). One key asymmetry is that the LLW winds that enter the continent in the equatorial Congo separate the harmattan trade winds in the north from the Indian Ocean trade winds in the south. The common view in the 1980s was as follows (Leroux 2001; Taljaard 1972, 1981, 1986; Torrance 1979): the LLW was deemed to be a recurvature of the South Atlantic trade winds, and so in the boreal summer, the convergence of the LLW with the harmattan winds over the Sahel was deemed to be the ITCZ. However, since both the LLW and the Indian Ocean trades originated in the Southern Hemisphere, their confluence was not considered to be an ITCZ, and instead was labeled the "Congo air boundary." Meanwhile, the ITCZ was defined as the convergence of the LLW with the harmattans in North Africa, of the LLW with the northeasterly monsoon winds in East Africa, and of the southeasterly trades with the northeasterly monsoon in Tanzania and northern Mozambique.

Taljaard (1953) first identified both summer convergence zones as possible candidates for the ITCZ, and identified the southernmost (the CAB) to have a more distinct discontinuity in atmospheric properties. However, later works, including Thompson (1965) and Torrance (1979), made a clear delineation between the ITCZ and the CAB. Most sources mark the summer position of the CAB as mostly zonally oriented, and with a slight southwesterly–northeasterly tilt, stretching from the Angolan coast to eastern Zambia. Summer CAB latitudes range over 20°–15°S. The winter CAB, usually pictured in July and August, is drawn at 10°S over Angola and tilts northeast to the rift valley at various inclinations. It is remarked upon by Torrance (1979) and Taljaard (1986) that the CAB is not a steady-state feature, but rather exhibits intraseasonal fluctuations north and south that can be associated with rainfall variability. Leroux (2001) describes the monthly average position of the CAB as it moves south in austral spring and north in austral autumn, and the role of

moving polar highs in controlling the anomalous CAB movement.

There is some ambiguity as to whether the CAB was understood to exist embedded within the tropical rain belt or along the southern edge of it. Both Leroux (2001) and Torrance (1979) contrast the high humidity Congo air with the drier, continentalized easterlies and suggest that precipitation occurs primarily to the north of the CAB. Leroux (2001) claims that the southern African easterly jet (AEJ-S) is associated with the trades and overlies the westerlies, inhibiting rainfall immediately to the north of the CAB as well. However, Taljaard (1986) and van Heerden and Taljaard (1998) describe the CAB as the mean location of the core of a broad zones where active weather dominates, and discusses tropical lows that travel westward along the CAB. However, tropical lows may only form within the moist air mass, and not on its edge (Howard and Washington 2018).

3. Circulation features

To ascertain whether the CAB as described above exists in the ERA-5 reanalysis, Fig. 2 shows the climatological mean and selected representative days of surface specific humidity and dewpoint for each month between August and December. From August to October, the picture described by the above sources clearly holds, with convergence between dry easterlies and moist southwesterlies along a band that stretches from the center axis of Angola to western Zambia. The humidity gradient and confluence zone are both broad in the climatological mean but remarkably sharp in the daily case studies, occurring over 100 km in places.

As the season progresses, the monthly mean specific humidity to the south of the CAB steadily increases. This is likely due to a combination of factors: the increased humidity of the easterly trades due to the warming SSTs in the Indian Ocean, reduced upper-level subsidence as the subtropical jet moves south leading to the injection of a lesser amount of dry air into the lower troposphere and the re-evaporation of the rain that falls as a result of events such as TTTs (Harrison 1984; Taljaard 1986). By November, there is no longer a strong humidity gradient between the equatorial LLW and the easterly trades. Nor is the convergence between these two air masses a bold feature of Fig. 2. Instead, in November and December the main humidity gradient is oriented northwest–southeast, from northern Namibia into Botswana. This humidity gradient is also associated with convergence, now between the trades and the southerly Namibian nocturnal low-level jet (Rife et al. 2010). In this paper, we will call this feature the KD
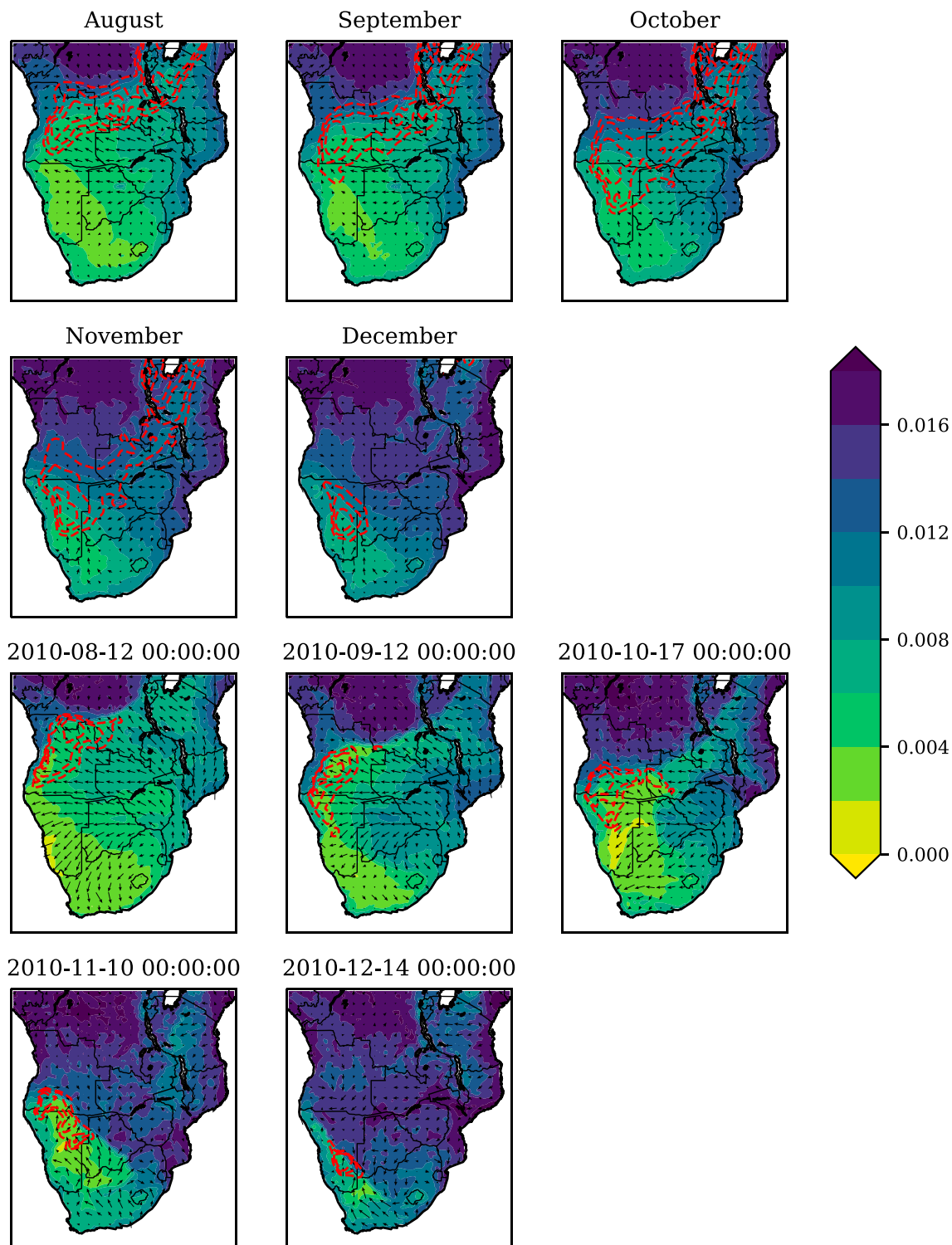
FIG. 2. (top),(top middle) Climatological mean and (bottom middle),(bottom) instantaneous surface conditions. Climatological mean 2-m specific humidity (kg kg^{-1}; colors), 100-m winds (arrows), and 1200 UTC 2-m potential temperature of the ($t_{\text{max-1}}$, $t_{\text{max-2}}$, $t_{\text{max-3}}$) (red contours). Columns indicate months.

(defined above) and will contrast its behavior and frequency with the CAB.

Figure 2 also shows contours of the locations of the maximum surface temperatures, which are consistently located immediately south of the CAB and to the west of the KD. This indicates a relationship between the surface discontinuities and the Angola and Kalahari heat lows, which will be further investigated in section 6.

To summarize, in late winter and early spring, the confluence of the equatorial LLW with the easterly trades over southern Africa shows up a clear discontinuity in the monthly and daily ERA-5 reanalysis data. In November and December, the humidity of the easterly trades increases and the two air masses appear to mix, such that the discontinuity is no longer immediately apparent. Thus the convectively active CAB featuring tropical lows as described by van Heerden and Taljaard (1998) may well exist in this season. However, it does not show up in daily ERA-5 data as an abrupt discontinuity, either in humidity or surface winds. As this study focuses on convergence and drylines, our algorithm will not detect this flavor of CAB. Instead, we focus in November and December on the KD farther south.

Criticisms of the use of the ITCZ paradigm over continental Africa are neatly summarized by Nicholson (2018), who argues that as the surface wind convergence maxima do not line up with the locations of the rainfall maxima, and so the traditional model of trade wind convergence setting the location of rainfall does not hold. It is easy to see why this is the case by examining Fig. 1—over the tropical rain belt, the relative humidity features very little gradient and is usually in excess of 95%. Thus, little wind convergence is required to reach saturation. However, surface wind convergence is collocated with the edge of the tropical rain belt, and so it is possible that the convergence zones of old are crucial in setting the location of the edge of the African rain belt. This paper will demonstrate that this is indeed the case for the southern edge of the rain belt in spring and early summer.

4. CAB identification algorithms

For the purposes of this study, the CAB is defined as a surface dryline and/or convergence line located at the northern edge of the easterly Indian Ocean trade winds, and the southern edge of the LLW. Similarly, the KD is a dryline or convergence line located at the southern edge of the Indian Ocean trade winds. Gradients in specific humidity were used to identify drylines over gradients in dewpoint temperature or relative humidity, due to the

former's conservation properties as per Hoch and Markowski (2005). However, replacing specific humidity with either dewpoint temperature or relative humidity gave similar results. Note that 100-m winds were chosen over winds on any pressure level because of the wide variation of surface pressures across southern Africa due to orography.

This section describes the method used to identify the CAB and the KD on a daily time scale in the ERA-5 reanalysis (Copernicus Climate Change Service 2017). First, strong gradients in relative humidity are identified each day using the Canny algorithm (Canny 1986). The algorithm is as follows:

1) Apply a Gaussian filter with a 0.5° radius to smooth the 2D surface specific humidity field q.
2) Calculate the gradient of the field ∇q.
3) Calculate the magnitude M and direction θ of the gradient such that $\nabla q = M \times [\sin(\theta), \cos(\theta)]$.
4) Calculate the right and left partial derivatives of M in the θ direction using the finite-difference method and using the closest horizontal, vertical, and diagonal axes. For example, if $0 \leq \theta \leq 45$, the formulas would be as follows:

$$\frac{\partial M}{\partial \theta^+} = \tan\theta[M(x+\delta, y+\delta) - M(x,y)]$$
$$+ (1 - \tan\theta)[M(x+\delta, y) - M(x,y)]$$

$$\frac{\partial M}{\partial \theta^-} = \tan\theta[M(x,y) - M(x-\delta, y-\delta)]$$
$$+ (1 - \tan\theta)[M(x,y) - M(x-\delta, y)]$$

5) Identify the locations where $\partial M/\partial \theta^+ \leq 0$ and $\partial M/\partial \theta^- \geq 0$. In the continuous limit, this would be equivalent to $\partial M/\partial \theta = 0$, implying the presence of a local maximum along the θ axis.
6) Return the locations where the above is satisfied and also $M > 0.003 \, \text{kg kg}^{-1}$ per grid cell.

The resultant locations are the Canny edges and will, by construction, be lines in the discrete 2D space with widths of 1 grid cell, as shown in the top center panel of Fig. 3. The colors in this figure indicate the angle θ. This procedure creates a set of points that are potentially locations of the CAB or the KD. To identify the CAB, these points are then filtered to retain locations where θ is between $-\pi/4$ and $\pi/6$ and is restricted to latitudes of 5°–18°S. To identify the KD, these points are then filtered to retain locations where θ is between $\pi/6$ and $\pi/2$ and is restricted to latitudes south of 12°S. Connected segments consisting of fewer than 10 grid cells
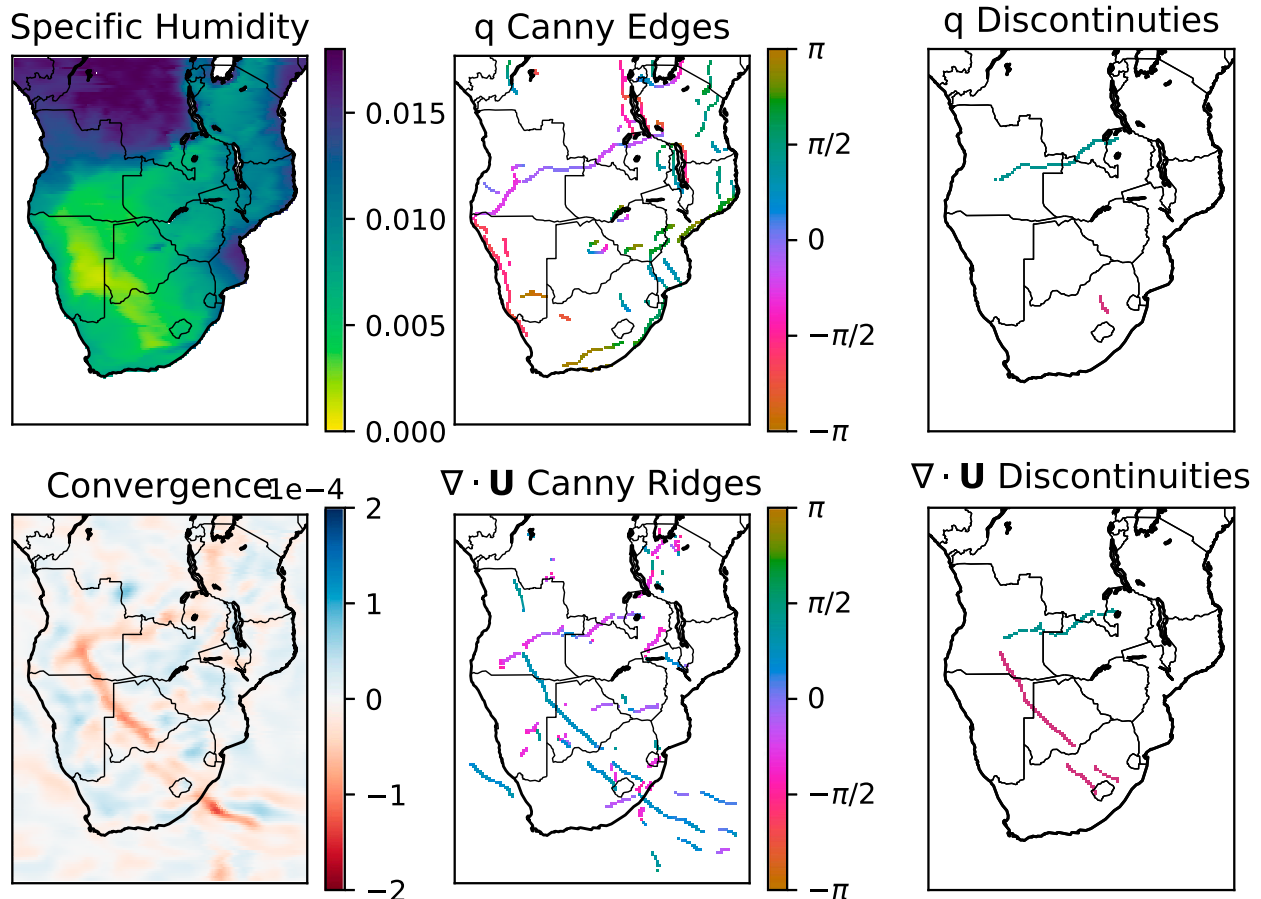
FIG. 3. Demonstration of the CAB and KD identification algorithm. (top left) 2-m specific humidity (kg kg^{-1}) on 25 Sep 2011. (top center) Corresponding Canny edges, with colors indicating edge orientation angle (radians). (top right) Dryline Canny edges that meet the CAB thresholds (green). No dryline KDs were identified for this day. (bottom left) The 100-m wind convergence on the 25 Sep 2011. (bottom center) Corresponding Canny ridges, with colors indicating edge orientation angle (radians). (bottom right) Convergence-line Canny ridges that meet the CAB thresholds (green) and KD thresholds (red).

are also deemed spurious and are removed from both definitions. These latitude and angle thresholds have been chosen carefully to include all instances of the CAB and KD while excluding spurious events associated with passing weather systems and coastal boundaries. These discontinuities will be referred to as the dryline CAB and the dryline KD from now on.

Convergence lines are identified using a similar method but detecting ridges in the convergence field rather than edges in humidity. This method combines the Canny (1986) algorithm with the approach of Weller et al. (2017) in identifying convergence lines. The Weller et al. (2017) method is used to find the angle of the convergence line, which allows the Canny (1986) method to be applied despite the fact that horizontal wind convergence is a scalar and so does not have an inherent direction associated with it, unlike the humidity gradient vector. The approach is as follows:

1) Apply a Gaussian filter with 0.5° radius to smooth the 100-m wind fields u and v and then calculate the convergence from these smoothed winds: $c = -\nabla \cdot \mathbf{u}$.

2) Apply a threshold to the convergence at a value of $2 \times 10^{-5}\,\text{s}^{-1}$ and split the remaining field into connected regions.

3) For each point with convergence above the threshold, compute the convergence inertia tensor using only points inside the enveloping connected region and within a box of 10 by 10 grid points, equivalent to $2.5° \times 2.5°$ [as per Weller et al. (2017)].

4) Compute the eigenvalues of the convergence inertial tensor. The angle of the eigenvector with the largest eigenvalue will be the orientation of the major axis of convergence at this point, and that of the smaller eigenvalue will be the orientation of the minor axis of convergence.

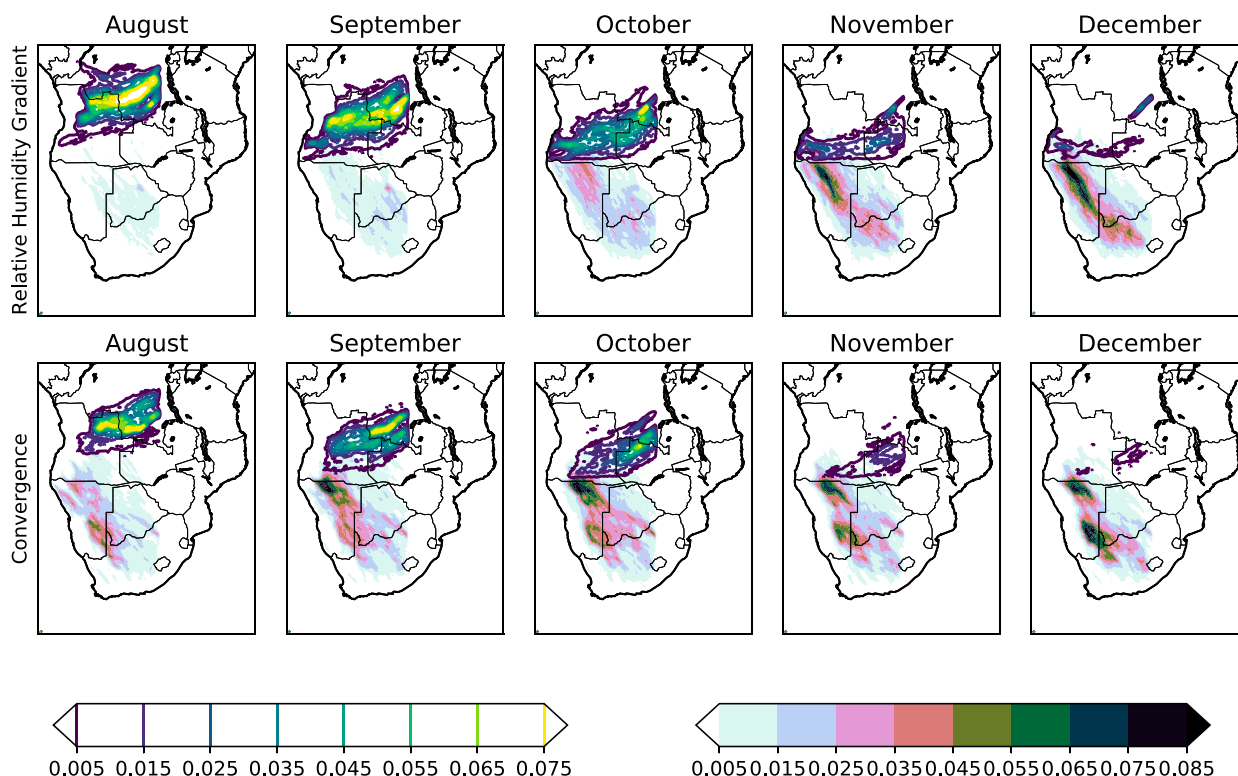Proportion of days when surface discontinuity identified at each grid point

FIG. 4. Climatological spatial distribution map of CAB and KD locations by month. (top) Dryline CAB and KD. (bottom) Convergence-line CAB and KD. Columns indicate months as labeled. Contour lines indicate the CAB; filled contours show the KD. Units are frequency per grid cell per month in each case.

5) Proceed as per steps 4–6 of the humidity algorithm, replacing θ with the angle of the minor axis of convergence and M with the magnitude of convergence.

Again the CAB and KD are identified from the resulting grid cells based on the angle, latitude, and minimum size criteria described earlier. We call these delineations the convergence-line CAB and the convergence-line KD. This gives two measures of where each discontinuity exists, as shown in the right column of Fig. 3. On a day that a CAB or KD exists, we define its center as the centroid of the largest connected set of flagged grid cells. The frequency of CAB and KD detection has been found to be sensitive to the thresholds applied throughout the algorithm. However, the other key properties of the CAB and KD considered in this paper, including seasonal and diurnal cycles, cross sections, and rainfall controls, remained qualitatively unchanged throughout a sensitivity analysis.

5. Properties of the CAB and KD

Having identified the CAB and KD using the methodologies described in section 4, this section presents statistics on their prevalence, location, and intraseasonal and interannual variability based on both the dryline and convergence-line formulations. We confirm that the CAB and the KD are real phenomena and not reanalysis artifacts by considering 17 AWSs, and we consider vertical north–south cross sections of composites around the centroid of the CAB.

Figure 4 shows monthly heat maps of the CAB and KD locations using the two identification methods described in section 4. The seasonal southward shift in the CAB latitude is easily seen as the locus moves from North Angola and the DRC in August through to south Angola in November. The frequency CAB also decreases over the season, lessening in October and being almost nonexistent by December. The dryline CAB is detected approximately 20% more frequently than the convergence-line CAB.

The convergence-line KD is evident in each month, and does not move substantially north–south or east–west. However, in August and September it is rarely associated with a dryline KD, and from October onward the dryline KD becomes more frequent. The dryline KD ramps up as both measures of the CAB ramps down,
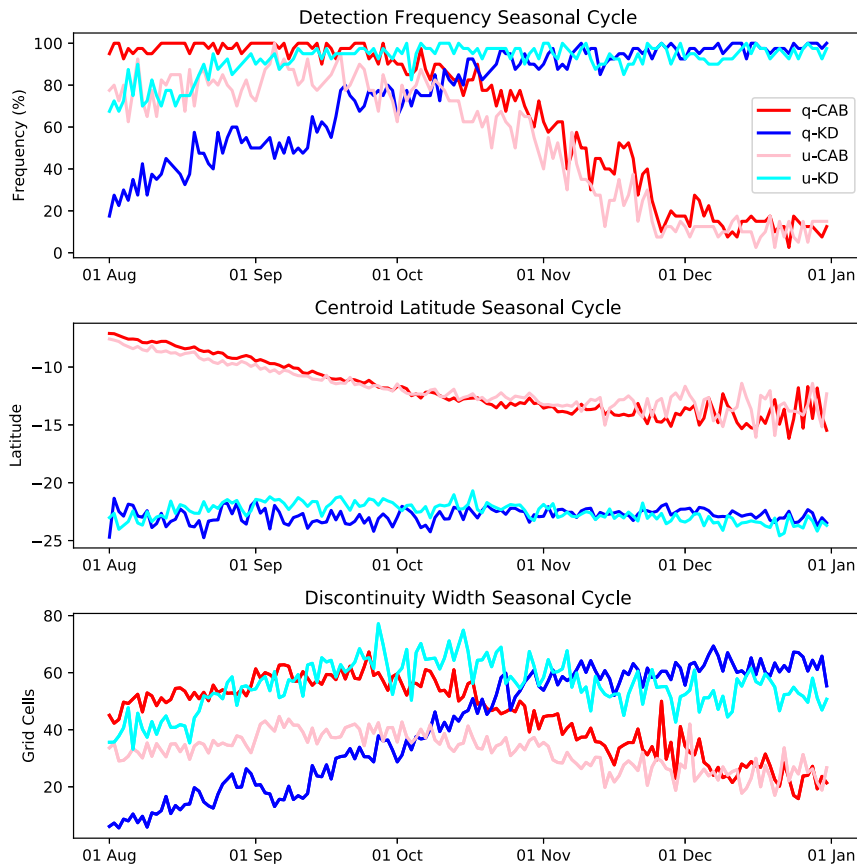
FIG. 5. (top) Climatological frequency that a CAB or KD is identified, by day of the year. (middle) Climatological mean latitude of the CAB and KD by day of the year. (bottom) Climatological mean number of CAB and KD grid cells identified on each day of the year. This is a measure of the length of the CAB. Dark blue: dryline KD; light blue: convergence-line KD; red: dryline CAB; pink: convergence-line CAB.

suggesting that the dryline KD replaces the dryline CAB in the later months.

These results are consistent with the seasonal cycles of latitude, frequency, and width shown in Fig. 5. The top panel of Fig. 5 demonstrates that the dryline CAB is usually always present in August and September, and its frequency declines over October and November, until it is rarely detected in December. The convergence-line CAB is consistently about 20% less frequent than the dryline CAB from August to November. Meanwhile, the dryline KD is present 20% of the time at the start of August, which increases to 100% by November.

The latitude of both CAB centroids, shown in the center panel of Fig. 5, moves steadily south from 7°S at the start of August to the start of November in a linear fashion, with a slope of 2° of latitude per month. At the start of November the latitude of the CAB levels out. There is a large amount of noise in the estimates of the CAB latitudes in December, which is likely due to the low frequency at which either CAB is detected in this

month. The bottom panel of Fig. 5 shows the climatological average number of CAB and KD grid cells identified each day of the year. This is a proxy for the length of the discontinuity; if the discontinuity was purely horizontal, then 40 grid cells would mean that a discontinuity was 10° long, for example. This measure follows a similar seasonal cycle to the frequency, with the CAB lengths decreasing over the season, and the KD lengths increasing. The convergence-line CAB is typically two-thirds as long as the dryline CAB from August to October. At all times, there is usually a dryline CAB or KD spanning on average 60 grid cells, equivalent to about 15°.

Thus we have shown that the CAB and the KD are significant features of the southern African spring climatology, with at least one present for more than 80% of days and often spanning one-half of the zonal extent of the continent. Figure 6 provides further insight into the vertical and diurnal structure of the CAB, showing vertical north–south composite cross sections of specific
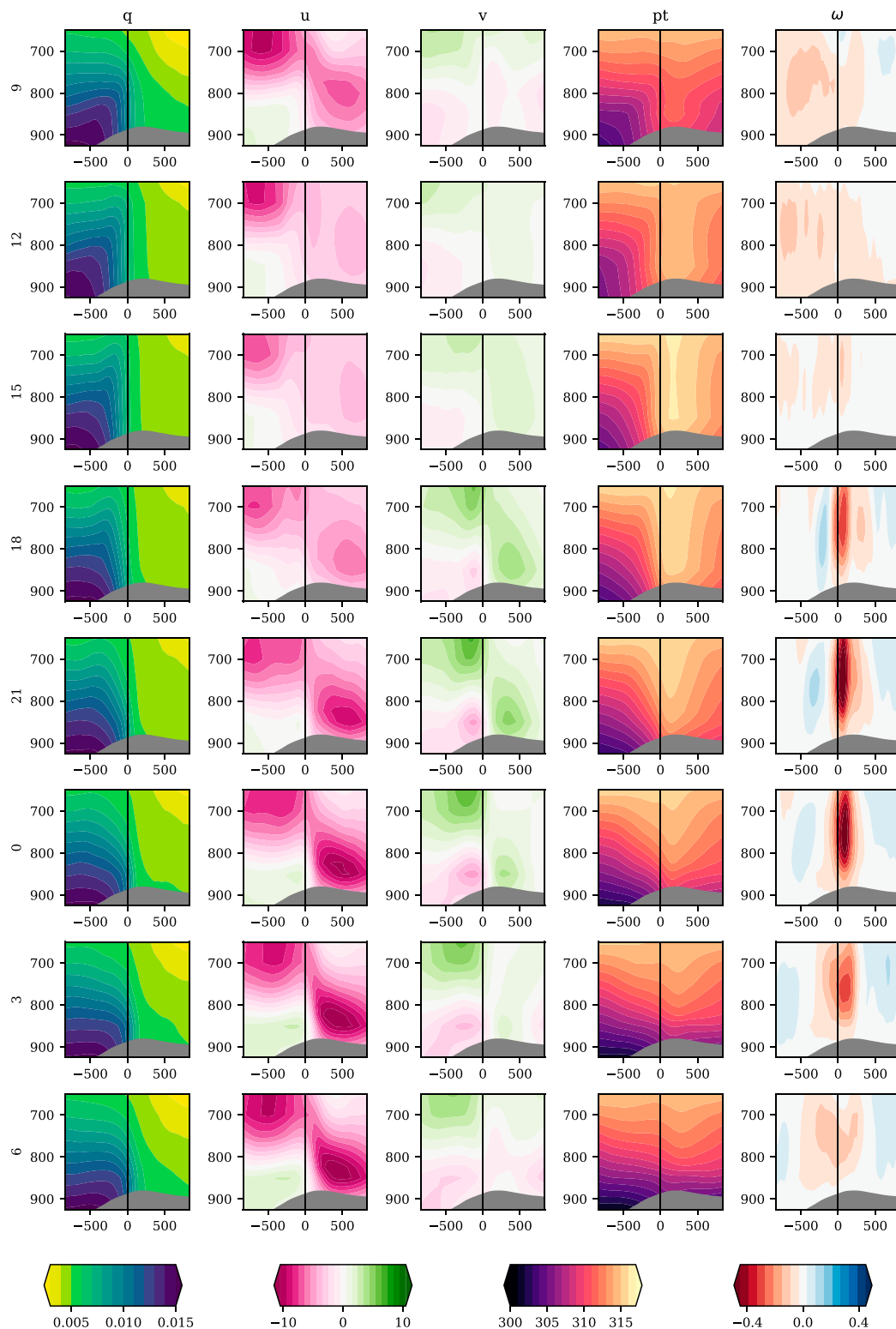
FIG. 6. Diurnal vertical north–south composites centered around the dryline CAB. Columns represent variables: specific humidity (kg kg^{-1}), zonal winds (m s^{-1}), meridional winds (m s^{-1}), potential temperature (K), and uplift (Pa s^{-1}). Rows indicate time of day (UTC) as labeled. The x axis is the displacement south of the CAB in kilometers, and the y axis is pressure.

humidity, zonal and meridional winds, potential temperature, and vertical velocity ω at 8 times of the day for the month of September. Equivalent east–west cross sections were examined for the dryline KD in November, and found to be qualitatively similar. These are not shown for brevity. The composites in Fig. 6 have been centered around the 0000 UTC position of the dryline CAB, located at $x = 0$ and indicated by the vertical black line. The region to the north of the CAB is displayed to the left of the black line, with high humidity, cooler temperatures, and northwesterly winds. Right of the black line is the region to the south of the CAB, with easterly winds, low humidity, and very high midday temperatures. The temperature maximum is located approximately 200 km south of the dryline CAB.

The strong meridional humidity gradient is present at all times of the day, but is strongest at midnight and weakest at midday. At 1200 UTC, surface wind speeds are low and the potential temperature profile is unstable, implying the presence of dry convection. Surface winds are suppressed by turbulent mixing, consistent with Parker et al. (2005). At 1800 UTC the atmospheric stability increases and the winds pick up, directed inward toward the temperature maximum and the center of the heat low (also apparent in Fig. 2). As they do so, the humidity maximum near the surface moves southward. Overnight, the surface winds rotate cyclonically, with winds to the south of the CAB shifting from southeasterly to easterly, and the winds to the north shifting from northerly to northwesterly. This is consistent with these winds being partially driven by the low-level thermally direct inflow of the heat low, which, under the influence of the Coriolis force, rotates overnight to form a cyclonic vortex (Rácz and Smith 1999; Howard and Washington 2018). In the morning, the surface temperatures increase and so turbulence builds and the winds are inhibited again. In the midtroposphere, the southern African easterly jet is present to the north of the CAB.

Uplift near the CAB is consistently negative (and so, upward), consistent with the collocation of the CAB and the heat low. However, somewhat counterintuitively, this uplift is strongest at night, and not in the morning when the atmosphere is most thermally unstable. We hypothesize that this is because the daytime convection is not explicitly resolved by the reanalysis model, and is instead provided by the turbulence scheme. This subgrid-scale dry convection is not included in the ω term, which only represents the explicitly resolved uplift associated with the wind convergence of the resolved horizontal winds, such that the continuity equation is closed. We shall return to this hypothesis in section 6.

Before proceeding further, we wish to address the possibility that these drylines and convergence lines are reanalysis artifacts as opposed to being features of the true atmosphere. The number of observations being fed into reanalysis products in tropical southern Africa is limited, and so the reanalysis products rely heavily on their modeled components and assimilation schemes in these regions. Therefore, we study the representations of the CAB at eight AWSs in the Southern African Science Service Centre for Climate Change and Adaptive Land Management (SASSCAL) network (http://www.sasscalweathernet.org) across Angola and Zambia, and the KD at nine stations across Namibia and Zambia (Helmschrot et al. 2015). Summaries of these sites are given in Table 1, and a map of their locations is shown in Fig. 7. The eight CAB sites are labeled in order of decreasing latitude, and the nine KD sites are labeled by increasing longitude.

Like all AWS networks, the SASSCAL dataset is spatially sparse and all of the stations are located within their own microclimates, which may not necessarily be comparable. Therefore, we consider the change in the measured weather condition as the reanalysis defined CAB or KD passes from north to south or from east to west, respectively, of each station, rather than trying to identify spatial gradients between stations. For each of the eight northern SASSCAL sites along the CAB, days were identified during which a dryline CAB grid cell was identified in the reanalysis either directly north or directly south of the station. Similarly for the nine southern sites along the KD, days were identified when a dryline KD was east or west of the station. The upper two rows of Fig. 8 then shows a scatterplot of the midnight recorded specific humidity against dryline CAB latitude at the station longitude. Data points represent all days when the CAB was present at this longitude and that data were available from the AWS. The marker colors show the 1200 UTC potential temperature recorded at the station the day before. The lower three rows show similar scatterplots for the KD, replacing the north–south axis with an east–west one, and transposing the plots so that longitude is shown on the x axis.

At all the stations, there is a transition as the CAB moves past the station—shown with a black line—from having lower humidity when the CAB is to the north of the station to higher humidity when the CAB is to the south. Likewise, there is a transition as the KD moves past the station from having lower humidity when the KD is to the east of the station to higher humidity when the KD is to the west. The suddenness of this transition indicates the sharpness of the CAB or KD, and it varies across the stations. In most cases, the transition occurs

TABLE 1. SASSCAL stations used in this study. The columns for number of days indicate data availability between August and December only.

Index	Name	Logger identifier	Country	Lon	Lat	n days (dry)	n days (wet)
1	Muconda	E12477	Angola	21.3°E	10.6°S	50	51
2	Mwinilunga	856121	Zambia	24.4°E	11.7°S	94	202
3	Copperbelt University	858854	Zambia	28.2°E	12.8°S	31	95
4	Zambezi	856126	Zambia	23.1°E	13.5°S	92	253
5	Cusseque	858129	Angola	17.1°E	13.7°S	55	83
6	Dongwe	361095	Zambia	24.0°E	14.0°S	31	152
7	Kafue National Park-Tatayoyo	858244	Zambia	24.4°E	14.9°S	14	175
8	Kalabo	856135	Zambia	22.7°E	15.0°S	31	311
9	Orongo	31212	Namibia	15.3°E	17.7°S	252	119
10	Erichsfelde	31197	Namibia	16.9°E	21.6°S	463	102
11	Kalahari	112	Namibia	18.5°E	24.2°S	345	45
12	Sonop	31213	Namibia	18.9°E	19.0°S	129	376
13	Sandveld	31198	Namibia	19.1°E	22.0°S	311	254
14	Tsumkwe	31204	Namibia	20.4°E	19.6°S	85	382
15	Ghanzi	68204	Botswana	21.7°E	21.7°S	103	203
16	Tsabong	31204	Botswana	22.4°E	26.0°S	195	113
17	Mogobane	23	Botswana	25.7°E	25.0°S	72	165

over less than 5°. In some, such as Zambezi, Muconda, Ghanzi, and Mogobane, the transition occurs within 1°–2°.

The point colors at all stations in Fig. 8 indicate that the warmest temperatures occur when the CAB and KD are respectively located 0°–5° to the north and east of the station. This is consistent with Figs. 2 and 6, which also show that a potential temperature maximum occurs immediately south of the CAB and west of the KD. Together with the results from specific humidity, this suggests that the CAB, as identified in ERA-5 re-analysis, is evident with the SASSCAL AWS dataset. Similar analysis of SASSCAL 10-m winds (not shown) has found that wind direction at 11 out of 17 stations notably changed direction on either side of the CAB. Considering that the measured winds are likely to be particularly susceptible to the microclimates of the station locations, this suggests that the CAB and KD winds as represented in ERA-5 reanalysis are consistent with the observed atmosphere.

6. Moisture budget analysis of the diurnal cycle

The consistent proximity of the CAB and the edge of the rain belt to the surface potential temperature maximum in Figs. 1, 6, and 8 suggests that there is a link between the location of the Angola heat low and the CAB. Such a link would provide a mechanism by which the Angola heat low influences the progression of rainfall onset in southern Africa, as noted by Dunning et al. (2018). In this section, the relationship between the heat low and the CAB is explored using a moisture budget analysis.

The formulation of the moisture budget used in this paper is as follows:

$$\underbrace{\partial q / \partial t}_{\text{Tendency}} = \underbrace{-\mathbf{u}_h \cdot \nabla_h q}_{\text{Horizontal Advection}} - \underbrace{\omega \partial q / \partial p}_{\text{Vertical Advection}} \underbrace{- c - \nabla \cdot q' \mathbf{u}'}_{\text{Residual}},$$

(1)

where q, $\mathbf{u}_h$, and ω are the resolved specific humidity and horizontal and vertical winds respectively, in pressure coordinates, and q' and $\mathbf{u}'$ are the subgrid-scale eddy specific humidity and 3D winds. The left-hand term represents the time derivative of specific humidity, the first term on the right its advection by large-scale horizontal winds and the second vertical advection. In the
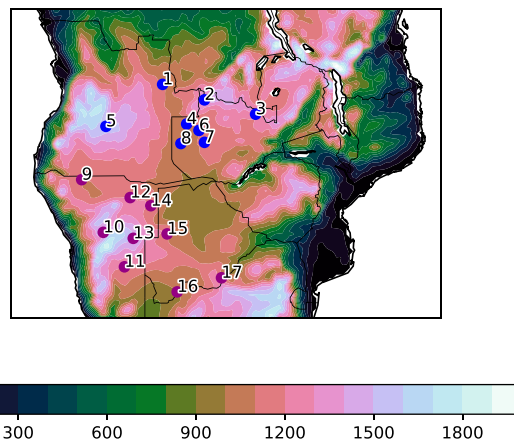

FIG. 7. SASSCAL site locations, labeled as per Table 1. Colors indicate surface altitude (m). Blue indicates sites used to study the CAB. Purple indicates sites used to study the KD.
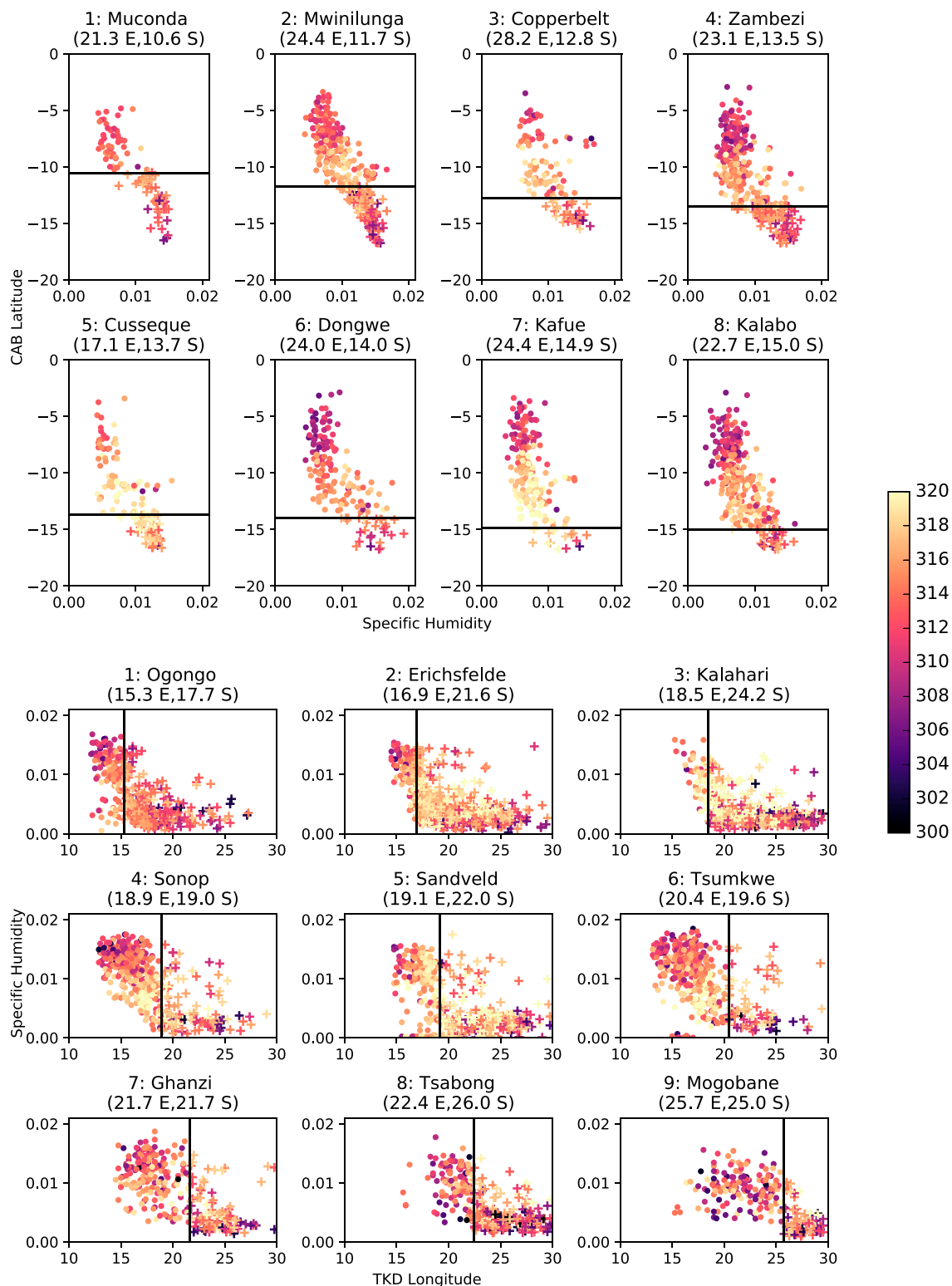
FIG. 8. (top),(top middle) Scatterplots of SASSCAL specific humidity (kg kg^{-1}) against reanalysis dryline CAB latitude (°) for days on which the dryline CAB exists at the same longitude as the station. Panels indicate stations as labeled in Table 1; the *x* axis represents measured 0000 UTC specific humidity at the station, and the *y* axis is the latitude of the CAB at the station longitude. Colors indicate the measured potential temperature at the stations (K). The black line is the station latitude. Stations are presented horizontally in order of decreasing latitude. Dots or plus signs show data points north or south, respectively, of the CAB. (middle),(bottom middle),(bottom) As in the top two rows, but for the KD, with the *x* axis showing reanalysis KD latitude and the *y* axis showing 0000 UTC measured specific humidity.

third term, the residual, c represents the addition and removal of moisture from the atmosphere by evaporation and precipitation such that $\int_{p_s}^{0} c \, dp = E - P$. The second component of the residual represents the unresolved moisture transport by turbulent processes. This will be dominated by the vertical term, $\partial q' \omega' / \partial p$, representing subgrid-scale convection, turbulent mixing, and boundary layer growth.

Figure 9 shows composites of the diurnal moisture budget terms, averaged around the centroid of the CAB. Evidently, the residual term dominates the moisture budget during the day. Horizontal advection is minimal since the horizontal winds are suppressed by turbulent mixing (Fig. 6) (Parker et al. 2005). The spatial distribution of the residual term, as a moisture sink near the surface and a moisture source aloft, is representative of boundary layer growth driven by dry convection. In the early afternoon, the stratification of potential temperature is unstable (Fig. 6), meaning that dry subgrid-scale convection is occurring and fueling boundary layer growth. This residual term largely contains advection of moisture by subgrid-scale uplift and far exceeds the uplift due to resolved ω (third column). This confirms our hypothesis from section 5 that the uplift associated with the heat lows is unresolved by the reanalysis and instead is dealt with by the turbulence scheme. Specific humidity decreases in the lower atmosphere and increases aloft as moisture is lifted throughout the day. Boundary layer growth has its highest vertical extent 200 km south of the CAB. Comparing to Fig. 6, this is the center of the heat low, the location of maximum surface potential temperature and the maximum thermal instability.

In the evening and overnight, the turbulent fluxes die down and the tendency is balanced by horizontal advection. The impact of this advection is to advect the specific humidity south at the latitude of the CAB. Comparing to Fig. 6 and remembering that the horizontal advection term is calculated as $u(\partial q / \partial x) + v(\partial q / \partial y)$, we conclude that the advection is driven by the southward component of the wind centered at 850 hPa to the north of the CAB (Fig. 6, third column), as they pass across the humidity gradient. The next morning, the boundary layer grows again, the horizontal winds (and hence horizontal advection) are suppressed, and the process is repeated.

Thus, the potential temperature maximum is intrinsically linked with the diurnal cycle of the CAB. During the day, vertical mixing associated with the unstable temperature profiles at the potential temperature maximum decreases the specific humidity near the land surface by mixing it upward. Overnight, the northwesterly winds associated with the LLW strengthen and

advect moisture on the southern edge of the CAB southward. As the LLW are driven by differential heating south of 6°N (Pokam et al. 2014), this process is also associated with the temperature maximum. Thus, by increasing and decreasing the humidity either side of the CAB edge, the heat low maintains the sharp humidity gradient.

A similar moisture budget analysis was performed for the KD in November, and the maintenance mechanism and diurnal cycle were qualitatively similar. In this case, it is the Kalahari heat low that maintains the humidity gradient.

7. Implications for rainfall over Southern Africa

The CAB and the KD both divide the hot dry air to the south from moist, often saturated air to the north, both at the surface and aloft (Fig. 6). It is clear, therefore, that in the vicinity of these discontinuities, rainfall ought only to occur to the north, as air to the south is far from saturated. Therefore, the locations of the CAB and the KD have the potential to exhibit control on interannual rainfall. It is nevertheless well established that tropical rainfall may occur in subtropical southern Africa, in the form of TTTs (Harrison 1984; Hart et al. 2013). In this section we determine the degree to which interannual variability of the CAB contributes to interannual variability of southern African spring rainfall, and investigate the relationship between the CAB, the KD, and TTTs.

First, we consider the interannual relationship between the dryline CAB latitude and frequency for each month from August to December. The top two rows of Fig. 10 show regressions of monthly precipitation on the monthly mean frequency and latitude of the CAB. Precipitation is calculated as the Climate Hazards Group Infrared Precipitation with Station (CHIRPS) monthly mean between 15° and 25°E, and between the 10th-percentile range of the daily CAB location in that month and 25° (Funk et al. 2015). In August and September, when the CAB frequency is always close to 100%, the monthly precipitation is strongly anticorrelated with the CAB latitude ($p < 0.001$; $r = -0.55$ and $r = -0.59$, respectively). From October to December, the precipitation becomes anticorrelated with the CAB frequency ($p < 0.001$; $r = -0.70$, $r = -0.58$, and $r = -0.69$, respectively).

Together, these results imply that the CAB plays a primary control on the spring and early summer rainfall in southern Africa. Early in the season, more rainfall may occur in this region when the CAB is farther south. Later, as the CAB begins to break down, there is more rain when the CAB is less frequent, as the moist air is
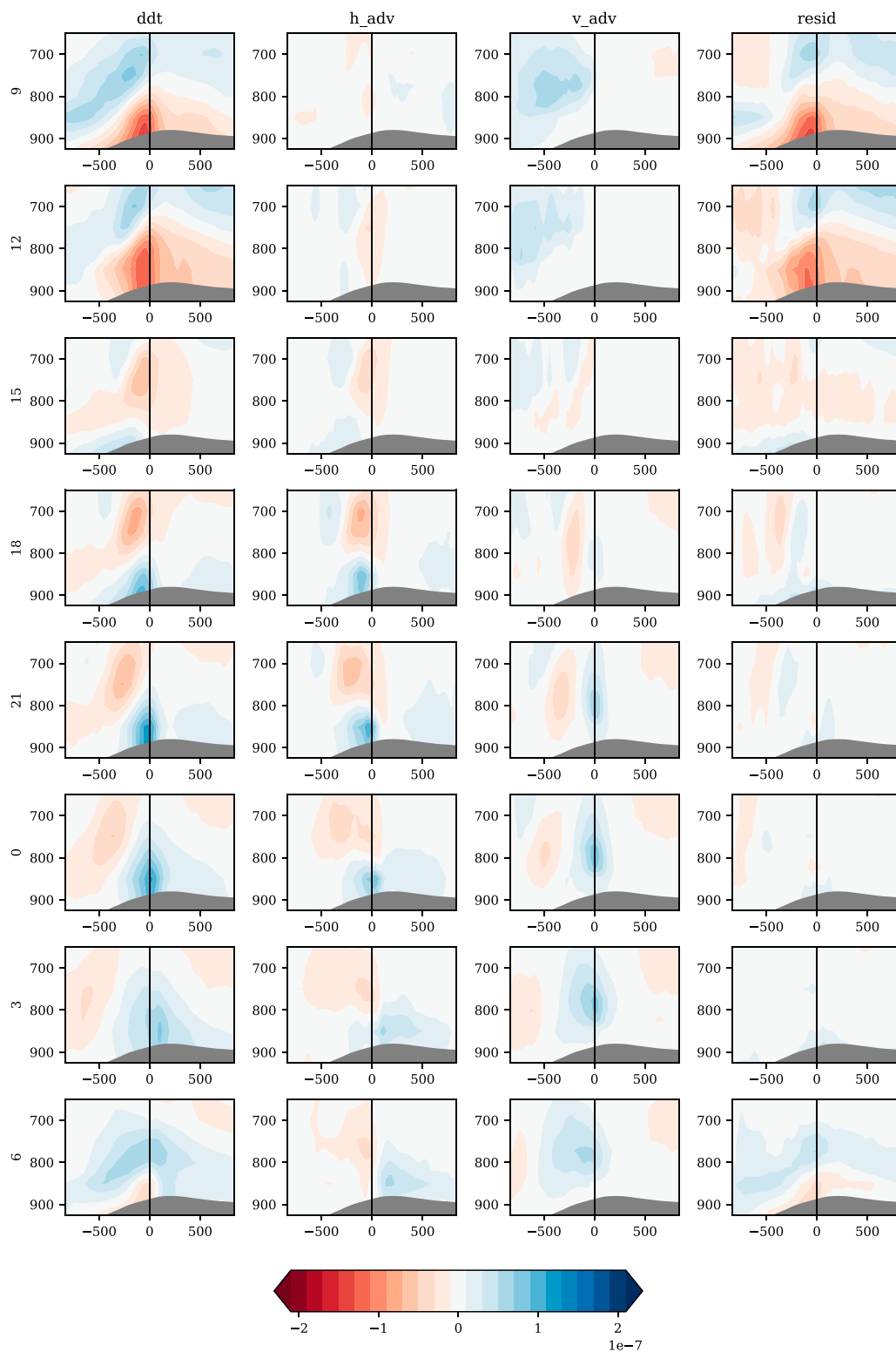
FIG. 9. As in Fig. 6, but the columns represent terms in the moisture budget ($kg\,kg^{-1}\,s^{-1}$): horizontal advection, vertical advection, time derivative, and residual (turbulent transport + rainfall).
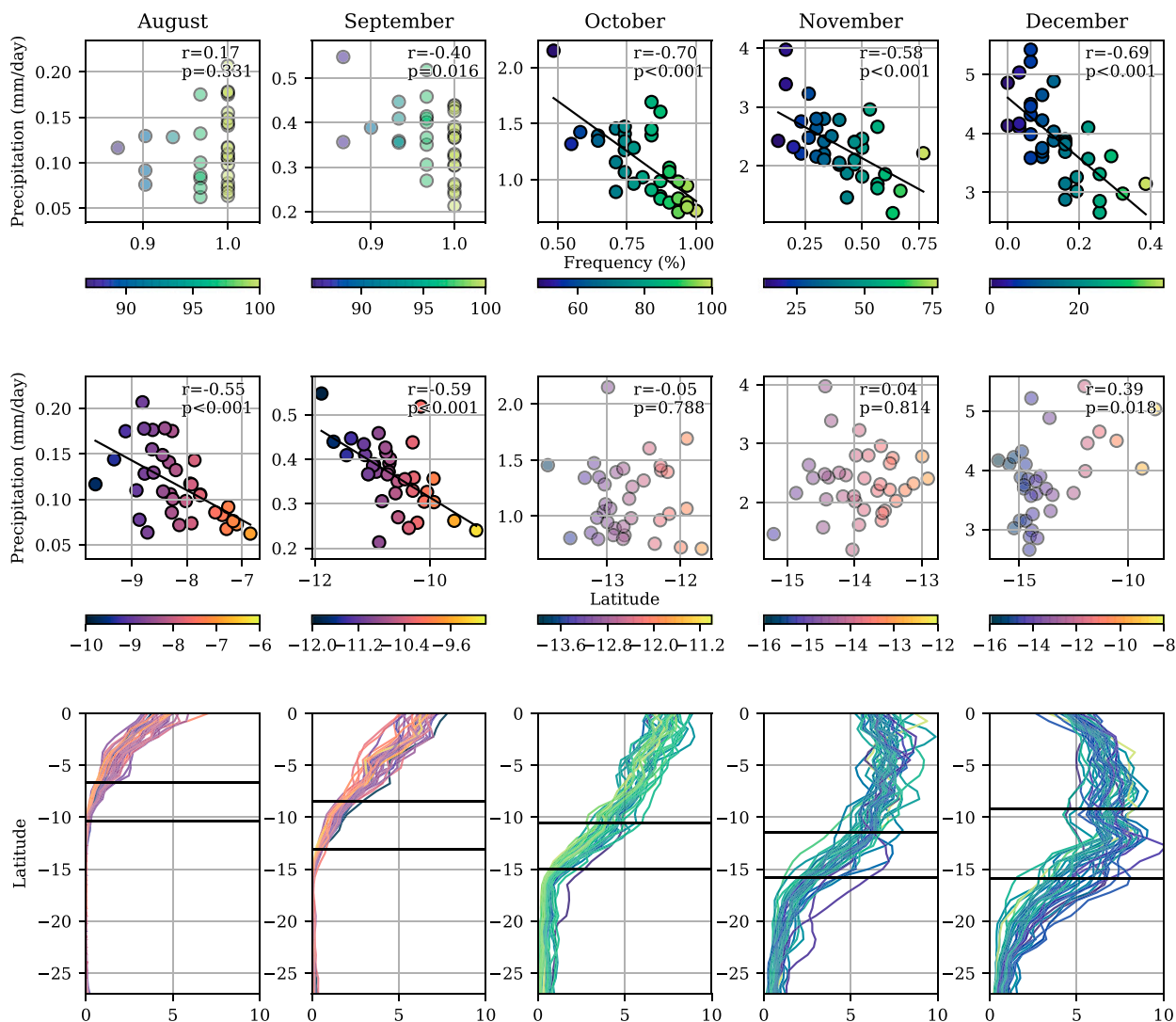
FIG. 10. Interannual rainfall variability due to the CAB. The columns indicate month. (top) Regression of rainfall onto CAB frequency. Rainfall is averaged from CHIRPS between longitudes 15° and 25°E and between the 10th-percentile CAB latitude and 25°S. The *x* axis indicates frequency; the *y* axis is precipitation (mm day^{-1}). The black line indicates the linear regression of rainfall onto CAB monthly mean CAB latitude when the regression is significant at a $p < 0.001$ level. Colors also indicate CAB frequency for greater clarity. (middle) As in the top row, but with precipitation regressed on CAB latitude. (bottom) Latitudinal profiles of monthly rainfall for each year between 1981 and 2015. Line color indicates CAB latitude (August and September) and CAB frequency (October–December), using the scales in the first two rows. The *x* axis is precipitation (mm day^{-1}), and the *y* axis is latitude. Horizontal black lines represent the 10th- and 90th-percentile latitude of the dryline CAB based on daily data in a given month. Rainfall is averaged between 15° and 25°E.

able to move farther south into the subtropics. We also found a relationship between the longitude of the dryline KD and rainfall in the same region in October and December ($p < 0.01$; $r = -0.46$ and $r = -0.55$, respectively), with less rainfall when the KD is farther east (scatterplots not shown). Note that the northernmost latitude of the averaging domain varies among climatological months, but not from year to year. This range is 6.7°S in August, 8.5°S in September, 10.6°S in October, 11.4°S in November, and 9.2°S in December.

The relationship between precipitation and the CAB latitude and frequency is evident across all latitudes of the averaging domain, as shown in the lower panels of Fig. 10. For each months, the edge 10th- and 90th-percentile ranges of the daily CAB location (black lines) enclose the southern edge of the tropical rain belt, where the slope of the precipitation is strongest. In this region, coloring of the profiles changes from light to dark across the figure from left to right. The coloring of the August and September panels corresponds to the CAB latitude,
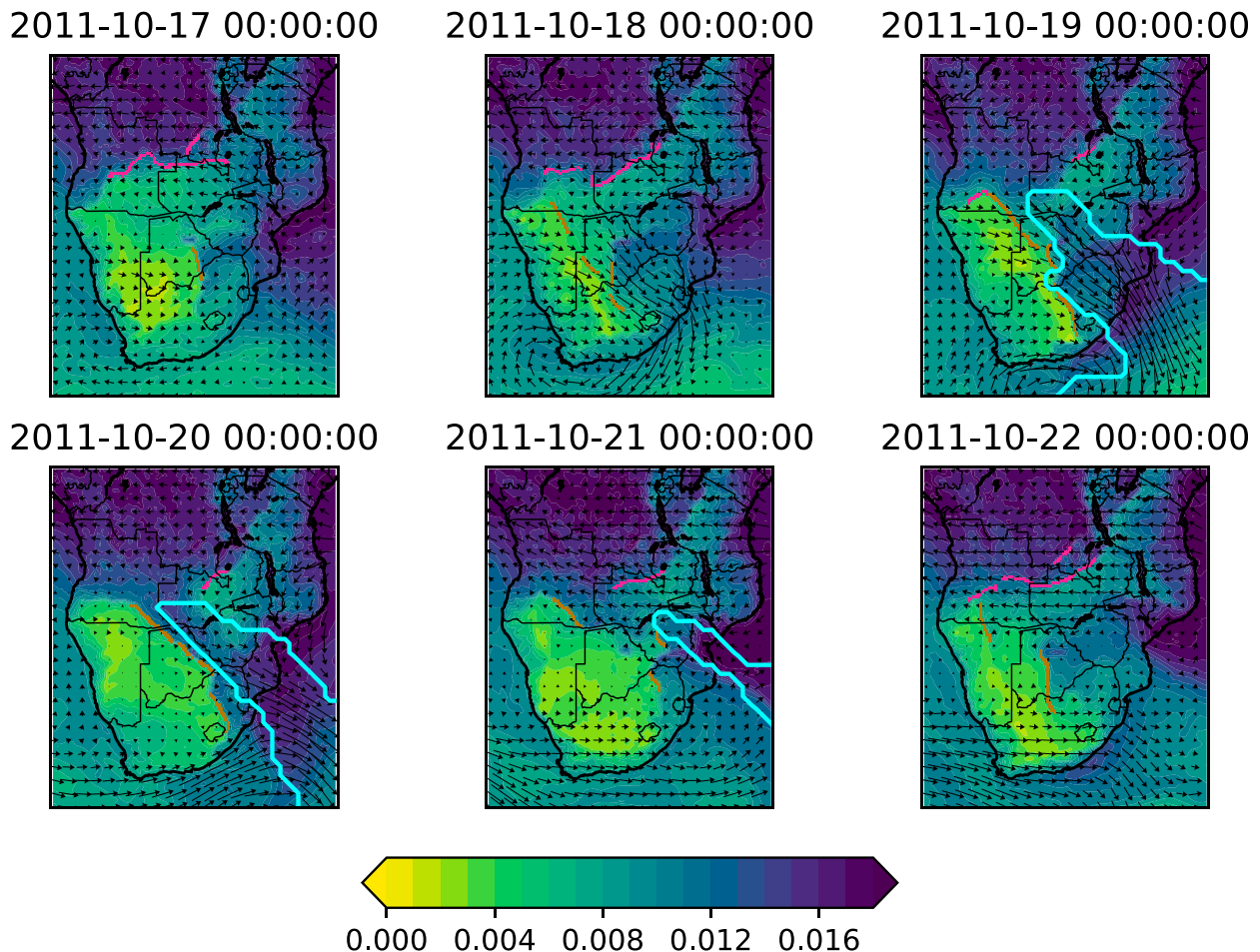
FIG. 11. Surface specific humidity and integrated moisture flux on the days surrounding a TTT event. Colors: 2-m specific humidity (kg kg^{-1}). Pink lines: dryline CAB. Brown lines: dryline KD. Blue contours: TTT envelope. Vectors: Column-integrated moisture flux.

as per the center row of panels, and that of October–December corresponds to CAB frequency.

In August to September, rain to the south of the P90 CAB line is close to zero in Fig. 10. From October to December, however, 0–1.5 mm of rain falls in this region per day. As the primary source of rainfall in subtropical southern Africa in summer is TTTs, we hypothesize that these weather events are the main source of this rainfall. Since both are key features of the spring climate of southern Africa, we wish to investigate the relationship between TTTs and the CAB, along with the KD.

A case study example of the interaction between the dryline CAB, the dryline KD, and a TTT is shown in Fig. 11. The TTT commenced on 19 October 2011 (as identified by the MetBot; Hart et al. 2012) and lasted for 3 days. Two days before the TTT was identified, a dryline CAB was present near 11°S, cutting diagonally across Angola and into the DRC from the southwest to the northeast. The day before the TTT formed, a dryline

KD began to form along eastern Namibia and western Botswana, while the dryline CAB was unchanged. A subtropical cyclone was generating northerly moisture flux over Botswana and South Africa. On the day that the TTT formed, the dryline CAB weakened and split into two small components located to the northeast and southwest its previous position. The northern edge of the TTT envelope was located in between the two CAB components. The northerly moisture flux associated with the TTT connected the subtropical cyclone to the moist convective air that is usually trapped to the north of the CAB and allowing it to flow south. The KD formed the southwestern edge of the TTT. On the proceeding day, this setup persisted, with both the TTT and the KD shifted to the east. On the 21st, the TTT moved offshore and by the 22nd, the CAB had reformed along a single axis, and the KD had mostly broken down.

From this analysis, we conclude that this TTT was in part the result of the interaction of a cyclone associated
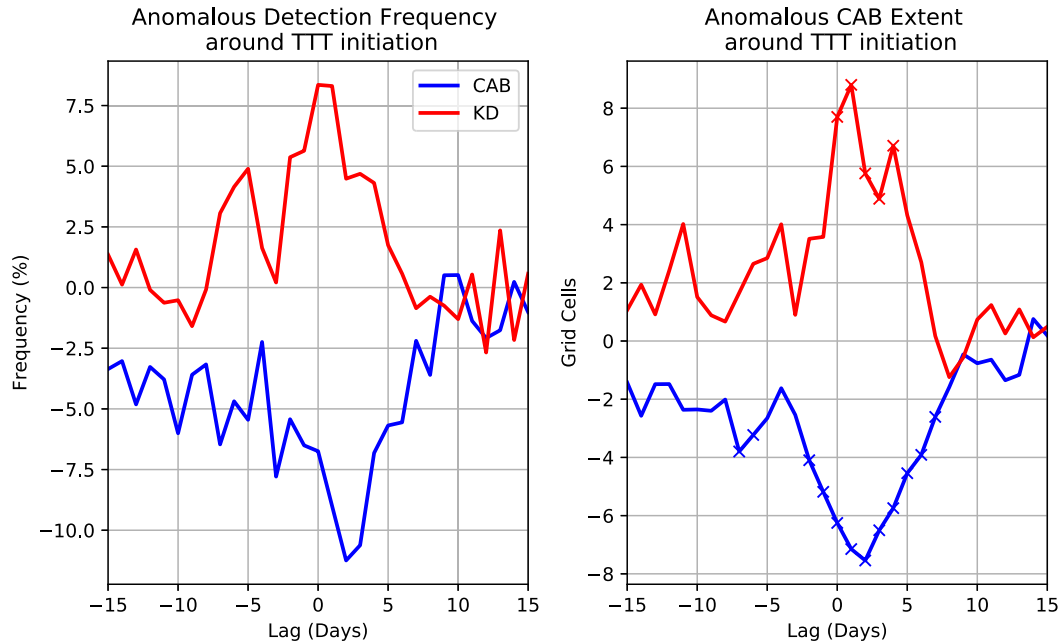
FIG. 12. Anomalous CAB and KD properties lagged around TTT flag date. (left) Anomalous frequency (%). (right) Anomalous number of grid cells identified per day. Anomalies have had the climatological seasonal cycle removed. Blue indicates dryline CAB; red indicates dryline KD. On the right panel, markers are shown where the result is significant at an $\alpha_{\mathrm{FDR}} < 0.05$ level, with the false discovery rate controlled for.

with the subtropical easterly jet breaking down the CAB and interacting with the moist tropical air to the north. The KD appeared to form in conjunction with the TTT, and it is possible that all the early season KDs are associated with TTTs in this manner. Figure 12 indicates that TTTs are associated with an increase in the frequency and length of the KD, and a decrease in the frequency and length of the CAB. Interestingly, the decrease in the CAB length becomes significant at an $\alpha_{\mathrm{FDR}} < 0.05$ level 7 days before the initiation of the TTT, suggesting that the CAB may be involved in the setup of TTT events. It appears that TTTs may be the result of an interaction of the CAB with a wave in the subtropical westerly jet (Macron et al. 2014) with the CAB, that causes the CAB to break down and a KD to form in its place, allowing Congo air to flow south to create the characteristic TTT southward moisture flux across the subtropical continent. Further work is required to verify this.

8. Discussion and conclusions

Surface drylines located along convergence lines at the edges of the easterly trade winds are persistent and important features of the southern African climatology. In spring, the dryline moves south with the trades along the CAB, forming a sharp boundary between the

tropics and the subtropics. As the subtropical easterlies become steadily more humid, the CAB dryline breaks down and is replaced with the KD, a southeast-to-northwest-oriented dryline along the edge of the Kalahari Desert in the west of the subcontinent. This dryline aligns with the southwestern extent of the easterly trade winds. A schematic of the typical climate features in play before and after the CAB breakdown is shown in Fig. 13.

We have found that properties of the CAB have significant and intuitive correlations with interannual rainfall over southern Africa. In the early season, the CAB latitude is strongly anticorrelated with rainfall averaged over the region that the CAB usually exists. This is likely to be a causal relationship, since saturated air may move and rain farther south when the CAB stretches farther over the continent. In the later seasons, the frequency of the CAB is anticorrelated with rainfall, such that more rainfall occurs when the CAB breaks down earlier. This relationship is more complex: it could be that the breakdown of the CAB allows more moisture to enter southern Africa from the Congo. However, it could also be the case that in seasons in which the low-level easterlies become more humid at a faster rate, due to Indian Ocean SSTs, a reduction in subsidence, or re-evaporation, the low-level easterlies cause both an increase in rainfall and the breakdown of the CAB. Most
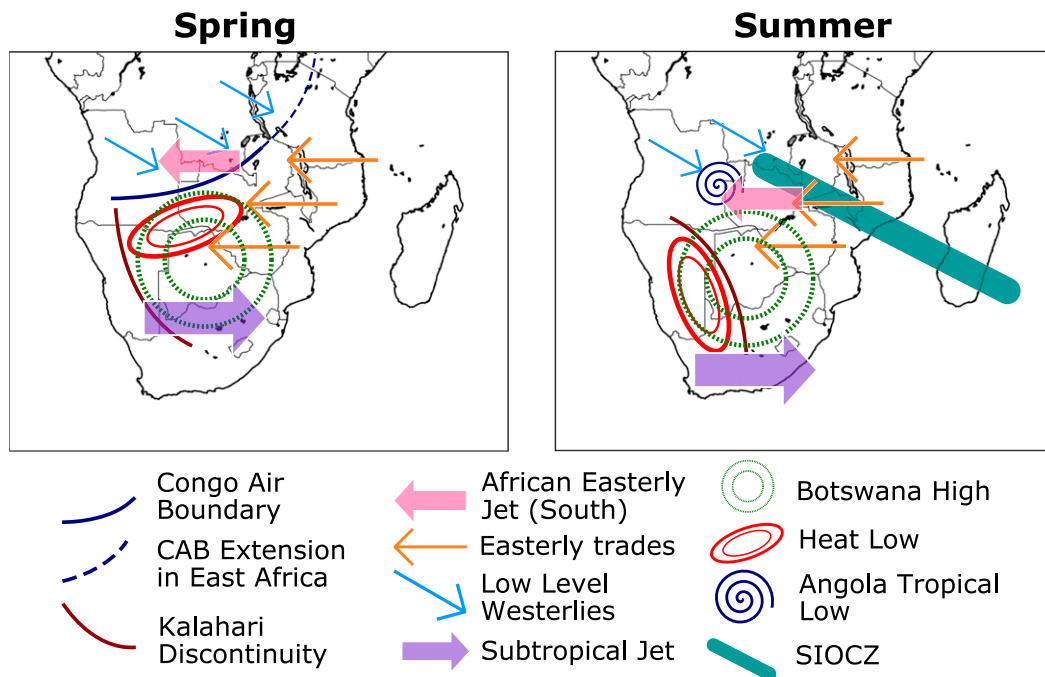
FIG. 13. Schematic of key features relating to the CAB and KD: (left) before the CAB breaks down (typically from August to mid-October) and (right) after the CAB breaks down (typically November and December). Features are as given in the legend and are not to scale. Locations are approximate. The extension of the CAB into East Africa has not been studied in this paper. In the left panel, the KD is a convergence line only and not a dryline.

likely, the correlation is due to a combination of these factors.

Interannual variability in southern Africa has previously been linked to other factors, including ENSO and the Atlantic and Indian Ocean highs. This paper does not claim that the CAB supersedes these drivers or precipitation. Rather, the CAB may be involved in teleconnection processes, and so may deliver remote signals on a synoptic time scale. Further investigation on the sources of interannual variability in the properties of the CAB and the KD is required, with particular focus on modes of variability deemed important for early wet season rainfall.

The KD is consistently located on the slopes of Namibia's Central Plateau, with the humid side downslope of the dry side. Similarly, the CAB climbs up from the Congo basin into Angola and Zambia over its seasonal cycle, and begins to disintegrating when it reaches the top of the plateau (Figs. 4 and 7). In other regions of the world, notably the U.S. Great Plains (Hoch and Markowski 2005; Jones and Bannon 2002), drylines also progress uphill over the season and the topography gradient has been described as the leading cause of the drylines. It is possible that topography also plays a role in maintaining the KD and the CAB.

A consistent collocation of drylines and surface potential temperature maximums has been observed throughout this paper. This suggests that the dynamics of these drylines may be closely linked with that of heat lows: the CAB with the Angola heat low and the KD with the Kalahari heat low. The winds that converge into the convergence-line CAB are, at least partially, driven by the direct thermal contrast set up by the heat low. By examining Figs. 6 and 9, we found that the overnight northerly winds associated with the Angola heat low's direct thermal inflow (Rácz and Smith 1999) advected the CAB south overnight, while subgrid-scale turbulent mixing, maximized in the unstably stratified core of the heat low, reduced the surface humidity at and ahead of the CAB during the day. Thus, the heat low maintains the sharp CAB gradient. Conversely, however, the dry and cloudless atmosphere to the south of the CAB and to the southwest of the KD has a relatively low heat capacity and high surface solar irradiation, and so is easy to heat up, meaning that the heat low may preferentially form on the dry sides of the CAB and KD. Thus, it is clear that the heat lows and drylines are intrinsically linked, and operate together.

The definition of the CAB in this paper was restricted to southern Africa with a near-zonal orientation. This was necessary in order to isolate the CAB from spurious features associated with lake boundaries, coasts, and weather events. However, it was noted by the authors

during the construction of the algorithm that the CAB drylines and convergence lines frequently extend diagonally eastward into East Africa. This can also be seen in Figs. 2, 3, and 11, and is consistent with early definitions of the CAB. Further analysis is necessary to examine the CAB in East Africa. Similarly, this paper has only considered the CAB in the austral spring and early summer; however, an investigation into whether it is also present in autumn and winter would be welcomed.

Future projections of climate change in southern Africa indicate that early season drying will be accompanied by an expansion of the Angola and Kalahari heat lows (Dunning et al. 2018; Cook and Vizy 2013). Given the close relationship between the heat lows and the CAB and the KD, this may cause a change in the behavior of the CAB and the KD in the future. These changes may be essential for a full understanding of the projected early season drying. The next step is to determine whether the CAB and the KD are represented in future climate models. The fidelity with which these features are simulated likely holds a vital key to confidence in climate model projections.

REFERENCES

Canny, J., 1986: A computational approach to edge detection. *IEEE Trans. Pattern Anal. Mach. Intell.*, **8**, 679–698, https://doi.org/10.1109/TPAMI.1986.4767851.

Conway, D., and Coauthors, 2015: Climate and southern Africa's water-energy-food nexus. *Nat. Climate Change*, **5**, 837–846, https://doi.org/10.1038/nclimate2735.

Cook, K. H., and E. K. Vizy, 2013: Projected changes in East African rainy seasons. *J. Climate*, **26**, 5931–5948, https://doi.org/10.1175/JCLI-D-12-00455.1.

Copernicus Climate Change Service, 2017: ERA5: Fifth generation of ECMWF atmospheric reanalyses of the global climate. Copernicus Climate Change Service, accessed 21 February 2019, https://cds.climate.copernicus.eu/cdsapp#!/dataset/reanalysis-era5-single-levels?tab=form.

Dunning, C. M., E. C. Black, and R. P. Allan, 2016: The onset and cessation of seasonal rainfall over Africa. *J. Geophys. Res.*, **121**, 11 405–11 424, https://doi.org/10.1002/2016JD025428.

——, ——, and ——, 2018: Later wet seasons with more intense rainfall over Africa under future climate change. *J. Climate*, **31**, 9719–9738, https://doi.org/10.1175/JCLI-D-18-0102.1.

Funk, C., and Coauthors, 2015: The Climate Hazards Infrared Precipitation with Stations—A new environmental record for monitoring extremes. *Sci. Data*, **2**, 150066, https://doi.org/10.1038/SDATA.2015.66.

Harrison, M. S. J., 1984: A generalized classification of South African summer rain-bearing synoptic systems. *J. Climatol.*, **4**, 547–560, https://doi.org/10.1002/joc.3370040510.

Hart, N. C. G., C. J. C. Reason, and N. Fauchereau, 2012: Building a tropical–extratropical cloud band metbot. *Mon. Wea. Rev.*, **140**, 4005–4016, https://doi.org/10.1175/MWR-D-12-00127.1.

——, ——, and ——, 2013: Cloud bands over southern Africa: Seasonality, contribution to rainfall variability and modulation by the MJO. *Climate Dyn.*, **41**, 1199–1212, https://doi.org/10.1007/s00382-012-1589-4.

Helmschrot, J., and Coauthors, 2015: SASSCAL WeatherNet to support regional weather monitoring and climate-related research in Southern Africa. *Proc. IAHS*, **366**, 170–171, https://doi.org/10.5194/piahs-366-170-2015.

Hoch, J., and P. Markowski, 2005: A climatology of springtime dryline position in the U.S. Great Plains region. *J. Climate*, **18**, 2132–2137, https://doi.org/10.1175/JCLI3392.1.

Howard, E., and R. Washington, 2018: Characterizing the synoptic expression of the Angola low. *J. Climate*, **31**, 7147–7166, https://doi.org/10.1175/JCLI-D-18-0017.1.

IPCC, 2013: *Climate Change 2013: The Physical Science Basis.* T. F. Stocker et al., Eds., Cambridge University Press, 1535 pp., https://www.ipcc.ch/site/assets/uploads/2018/02/WG1AR5_all_final.pdf.

Jones, P. A., and P. R. Bannon, 2002: A mixed-layer model of the diurnal dryline. *J. Atmos. Sci.*, **59**, 2582–2593, https://doi.org/10.1175/1520-0469(2002)059<2582:AMLMOT>2.0.CO;2.

Junginger, A., S. Roller, L. A. Olaka, and M. H. Trauth, 2014: The effects of solar irradiation changes on the migration of the Congo air boundary and water levels of paleo-Lake Suguta, Northern Kenya Rift, during the African Humid Period (15-5ka BP). *Palaeogeogr. Palaeoclimatol. Palaeoecol.*, **396**, 1–16, https://doi.org/10.1016/j.palaeo.2013.12.007.

Kizza, M., A. Rodhe, C. Y. Xu, H. K. Ntale, and S. Halldin, 2009: Temporal rainfall variability in the Lake Victoria Basin in East Africa during the twentieth century. *Theor. Appl. Climatol.*, **98**, 119–135, https://doi.org/10.1007/S00704-008-0093-6.

Lazenby, M. J., M. C. Todd, R. Chadwick, and Y. Wang, 2018: Future precipitation projections over central and southern Africa and the adjacent Indian Ocean: What causes the changes and the uncertainty? *J. Climate*, **31**, 4807–4826, https://doi.org/10.1175/JCLI-D-17-0311.1.

Leroux, M., 2001: *The Meteorology and Climate of Tropical Africa.* Springer, 548 pp.

Macron, C., B. Pohl, Y. Richard, and M. Bessafi, 2014: How do tropical temperate troughs form and develop over southern Africa? *J. Climate*, **27**, 1633–1647, https://doi.org/10.1175/JCLI-D-13-00175.1.

Nicholson, S. E., 1996: A review of climate dynamics and climate variability in eastern Africa. *The Limnology, Climatology and Paleoclimatology of the East African Lakes*, Gordon and Breach, 25–56.

——, 2018: The ITCZ and the seasonal cycle over equatorial Africa. *Bull. Amer. Meteor. Soc.*, **99**, 337–348, https://doi.org/10.1175/BAMS-D-16-0287.1.

NOAA, 2012: GPCP version 2.2 combined precipitation data set. NOAA/OAR/ESRL/PSD, accessed 21 March 2019, https://www.esrl.noaa.gov/psd/data/gridded/data.gpcp.html.

Parker, D. J., and Coauthors, 2005: The diurnal cycle of the West African monsoon circulation. *Quart. J. Roy. Meteor. Soc.*, **131**, 2839–2860, https://doi.org/10.1256/qj.04.52.

Pokam, W. M., C. L. Bain, R. S. Chadwick, R. Graham, D. J. Sonwa, and F. M. Kamga, 2014: Identification of processes driving low-level westerlies in west equatorial Africa. *J. Climate*, **27**, 4245–4262, https://doi.org/10.1175/JCLI-D-13-00490.1.

Rácz, Z., and R. K. Smith, 1999: The dynamics of heat lows. *Quart. J. Roy. Meteor. Soc.*, **125**, 225–252, https://doi.org/10.1002/qj.49712555313.

Rife, D. L., J. O. Pinto, A. J. Monaghan, C. A. Davis, and J. R. Hannan, 2010: Global distribution and characteristics of diurnally varying low-level jets. *J. Climate*, **23**, 5041–5064, https://doi.org/10.1175/2010JCLI3514.1.

Taljaard, J. J., 1953: The mean circulation in the lower troposphere over Southern Africa. *S. Afr. Geogr. J.*, **35**, 33–45, https://doi.org/10.1080/03736245.1953.10559299.

——, 1972: Synoptic meteorology of the Southern Hemisphere. *Meteorology of the Southern Hemisphere*, C. W. Newton, Ed., Amer. Meteor. Soc., 139–213.

——, 1981: Upper-air circulation, temperature and humidity over Southern Africa. South African Weather Bureau Tech. Paper 10, 94 pp.

——, 1986: Change of rainfall distribution and circulation patterns over southern Africa in summer. *J. Climatol.*, **6**, 579–592, https://doi.org/10.1002/joc.3370060602.

Thompson, B. W., 1965: *The Climate of Africa*. Oxford University Press, 15 pp., 131 maps.

Thyng, K. M., C. A. Greene, R. D. Hetland, H. M. Zimmerle, and S. F. DiMarco, 2016: True colors of oceanography. *Oceanography*, **29**, 9–13, https://doi.org/10.5670/oceanog.2016.66.

Tierney, J. E., J. M. Russell, J. S. Sinninghe Damsté, Y. Huang, and D. Verschuren, 2011: Late Quaternary behavior of the East African monsoon and the importance of the Congo air boundary. *Quat. Sci. Rev.*, **30**, 798–807, https://doi.org/10.1016/j.quascirev.2011.01.017.

Torrance, J. D., 1979: Upper windflow patterns in relation to rainfall in south-east central Africa. *Weather*, **34**, 106–115, https://doi.org/10.1002/j.1477-8696.1979.tb03418.x.

van Heerden, J., and J. J. Taljaard, 1998: Africa and surrounding waters. *Meteorology of the Southern Hemisphere*, D. J. Karoly, and D. G. Vincent, Eds., Amer. Meteor. Soc., 141–174.

Weller, E., K. Shelton, M. J. Reeder, and C. Jakob, 2017: Precipitation associated with convergence lines. *J. Climate*, **30**, 3169–3183, https://doi.org/10.1175/JCLI-D-16-0535.1.